Enhanced capacity and electrochemical performance of zinc cobalt selenide by using a novel two-stage synthesis method

Seied Ali Hosseini[*,1], Zeynodin Karami[2], Ali Olamaee[2], Morteza Saghafi Yazdi[2], Mohammad Abedini[2], Amirhossein Moghanian[2]*

[1]Department of Electrical Engineering, Faculty of Engineering, Imam Khomeini International University, Qazvin, Iran;
[2]Department of Materials Science and Engineering, Faculty of Engineering, Imam Khomeini International University, Qazvin, Iran.

*Corresponding author email: sahosseini@eng.ikiu.ac.ir

ABSTRACT

In this paper, a novel method of synthesis of zinc cobalt selenide (ZnCoSe) nanostructures via the hydrothermal method is introduced that is comprised of two stages as opposed to the direct method that could be done in a single stage. In the single-stage method, the consequent electrodes were covered by ZnCoSe that was directly and immediately synthesized while in the two-stage method, first, zinc cobalt oxide (ZnCoO) was hydrothermally produced then the oxygen atoms were replaced by selenium and the ZnCoSe* electrode was indirectly obtained. The structural and electrochemical evaluations showed boosted performance of the ZnCoSe* whose structure was found to be nanowire. In this paper, the specific capacitance values (C_{sp}) of the ZnCoSe* , ZnCoO and ZnCoSe electrodes were measured to be 104, 64 and 62 F.g^{-1} at 20 mV/s scan-rate by Cyclic voltammetry (CV) which alongside the Galvanostatic Charge-Discharge (GCD) analysis, led us to conclude superior activity of the ZnCoSe* electrode. Electrochemical impedance spectroscopy (EIS) was also performed and its results were in accordance with those of the cyclic voltammetry. Based on the EIS results, ZnCoSe* showed the smallest charge transfer resistance (6.5 ohm/cm^{-2}) and consequently the supreme electrochemical behavior among the studied electrodes. Moreover, a better capacity retention value was recorded in the cyclability test of the ZnCoSe* electrode as the specific capacity value of this electrode reached 145% of its initial value after 2000 cycles.

Keywords: *capacitance, electrode, zinc, selenide, cobalt, hydrothermal*

1. Introduction

Advanced technologies are rapidly being developed to harness energy in clean and renewable resources such as sun, wind and sea tides which are not perpetually accessible in every land and require development of energy storage methods and tools, especially batteries and supercapacitors. Furthermore, with the advent of digital devices such as cell phones, laptops, and electric or hybrid cars, the need to produce efficient electrical energy storages has been multiplied several folds. The most important devices that can store the electrical energy are batteries and supercapacitors.

One of the best energy storages are the supercapacitors (SC) because of their astonishing life time, rapid charging, substantial power density, cheapness, and easy manufacturing [1]. However, their wide usage is restricted due to their limited energy density (ED) [2]. To overcome this issue, it has been suggested that hybrid supercapacitors could be used in which activated carbon and metal sulfides/oxides are employed to provide suitable

power and energy sources.

The activated carbon hybrid supercapacitor works on basis of electrochemical double layer capacitance (EDLC) while the metal sulfides/oxides store charges according to principles of batteries or pseudocapacitors [3]. Rapid reversible redox reactions and multiple oxidation states of the battery-type materials make them superior to EDLC materials in terms of the electrochemical performance [4]. Thus, various metal oxides, selenides and sulfides were proposed to be used in supercapacitors to date [5, 6]. Among these three categories, unfortunately, metal oxides (MOs) have poor rate performance, stability, and electrical conductivity that makes them inappropriate for supercapacitors [7], but metal sulfides have been recommended for their excellent redox reversibility, low electronegativity, and better electrical conductivity [8]. Similar to sulfur and oxygen, selenium is in group 16 of the periodic table so it is reasonable to expect that they offer similar chemical characteristics, however in terms of electrical conductivity, selenium has shown to be a better conductor (10^{-3} Ω^{-1} m^{-1}) than sulfur and oxygen (Sulfur: 10^{-28} Ω^{-1} m^{-1}). Thus using selenium in combination with metals could be favorable because the higher electrical conductivity the higher charge-discharge capability of devices [9, 10]. Therefore recently, metal selenides have emerged as potential materials for energy storing applications such as batteries, fuel cells, solar cells, water splitting and SCs [11, 12].

As we are going to study zinc cobalt selenide, it is beneficial to cast a glance on zinc cobalt oxide too. Bimetals based on zinc and cobalt are vastly investigated. For example, Xu et al. synthesized porous $ZnCo_2O_4$ nanostructures via a simple hydrothermal route and heat treatment process. The synthesized electrode was a combination of nano-wires & nano-belts and exhibited great pseudocapacitive performance with a specific capacitance of 776.2 F g^{-1} at 1 A g^{-1} and good cycle stability (84.3% capacity retention at 3 A g^{-1}) [13]. Wang and co-workers prepared $ZnCo_2O_4$/rGO electrodes, which showed a specific capacitance of 626 F g^{-1} at 1 A g^{-1}, excellent rate capability with 81% retention of its initial capacitance at 30 A g^{-1}, and long-term cycling stability of 99.7% after 3000 cycles at 10 A g^{-1} [14]. $ZnCo_2O_4$@N-GO/PANi ($ZnCo_2O_4$@nitrogen doped graphene oxide/polyaniline composite) electrodes were synthesized by Kathalingam and co-workers. These electrodes

showed excellent electrochemical performance with ~720 F g^{-1} specific capacitance and cyclic stability above 96% after 10000 cycles [15]. Another investigation on $ZnCo_2O_4$ electrodes was recently published by Jadhav and co-workers. Their electrode offered specific capacitance of 746.3 F g^{-1} initially which increased up to 854 F g^{-1} after first 600 cycles and stayed stable for the next cycles up to the 6000th cycle. Specific capacitance of this electrode reached to 880 F g^{-1} after 6000 cycles and proved that such compounds are appropriate for practical use [16]. By study of the above works, one could conclude that Zn-Co oxide could be a suitable option for energy applications. Interestingly, in comparison with monometallic selenides (e.g. CuSe , VSe_2, $FeSe_2$, $NiSe_2$, and Co_3Se_4), bimetal selenides (e.g. $NiCo_2Se_4$, $Cu_{0.5}Co_{0.5}Se_2$, $CoFe_2Se_4$, and NiV_2Se_4) generally improve efficiency of charge storing due to the richer active centers they provide as a result of the powerful synergistic effects between the ions in the structure [17, 18].

Under shed of the above analysis, we studied bimetal selenides of ZnCoSe. Although there are some studies on the use of such materials in the literature, they are limited and there is room for their improvement. For instance, Cherbolu and co-workers synthesized nickel foam-supported (NF) ZnCoSe and reached the specific capacitance of 313.45 C g^{-1} (equivalent to 522.41 F g^{-1}) and the good cyclical stability of 95% over 3000 cycles . Another example is Cheng and their colleagues' work in which they investigated on hierarchical sea-urchin-like bimetallic zinc–cobalt selenide electrodes. They reported that their electrode exhibited a specific capacitance of 1419 C g^{-1} at 2 A g^{-1} and 83% capacity retention after 5000 cycles [19]. In table 1, we have summarized the results of the above-reviewed papers on ZnCoSe and ZnCoO.

Here, we report a novel two-stage method to fabricate ZnCoSe electrodes via a facile hydrothermal procedure. Throughout this paper, we have marked the electrode built with this novel procedure as ZnCoSe*. We have compared this novel electrode with normally built ZnCoSe electrodes and ZnCoO electrodes. We observed that all of the fabricated electrodes had significant properties for charge storing such as great cyclability, suitable energy delivery and high specific capacitance as well as binder-less fabrication method. These common features aside, we concluded that the ZnCoSe* device was superior to the other two electrodes in every way, thereby

Table 1- Comparison of the specific capacitance and capacitance retention among some similar energy storage devices

Material	Electrolyte	C_{sp} (F g^{-1})	Pot. Win. (V)	Discharge current (Ag^{-1})	Capacity retention% (cycle)	Ref
Zn–Co–Se	1 M KOH	522.41	0.4	0.5	95% (3000 cycle)	[1, 2]
ZnCo$_2$O$_4$	2 M KOH	776.2	-	3	84.3% (1500 cycle)	[3, 4]
ZnCo$_2$O$_4$/rGO	2 M KOH	626	0.45	1	81% (3000 cycle)	[5, 6]
ZnCo$_2$O$_4$@N-GO/PANi	3 M KOH	720	0.5	1.5	96% (10000 cycle)	[7]
ZnCoSe	3 M KOH	1419 (Cg^{-1})	0.6	2	83% (5000 cycle)	[8]
ZnCo$_2$O$_4$/NF	2 M KOH	880.5	0.8	12.5	103% (6000 cycle)	[9]

making this method of fabrication promising to be leveraged across other methods of electrodes in order to boost their performance.

2. Experimental Details
2.1. Materials

In this paper, urea (CO(NH$_2$)$_2$), cobalt chloride hexahydrate (CoCl$_2$·6H$_2$O), potassium hydroxide (KOH) and hydrochloric acid (HCl) were all purchased from Merck Chemical Reagent Co. and hydrated zinc nitrate (Zn(NO$_3$)$_2$·6H$_2$O) and ammonium fluoride (NH$_4$F) were obtained from Fluka Chemical Company.

2.2. Characterization Methods

In order to study the structures in the atomic scale, an X-ray diffractometer (XRD, Panalytical, USA) with step size of 0.04° to 2 θ s^{-1} (domain: 10°–70°) and radiation of Cu Kα (Kα, λ = 1.5406 A°) was used. A Fourier transforms infrared (FTIR) spectrometer was used to capture FTIR spectra (model: FTS-165, BioRad). Field emission scanning electron microscopy also found morphology of the materials (FE-SEM, Hitachi S4160, Emission voltage = 15 kV).
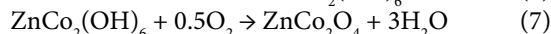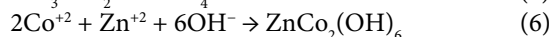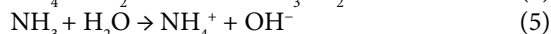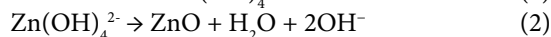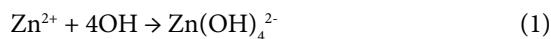
In order to electrochemically assess the electrodes, a potentiostat (Autolab, Ivium) was utilized. This device was used for capacity retention, GCD, and cyclic voltammetry experiments at different scan rates and in 1 M KOH as the electrolyte. The electrochemical impedance spectroscopy was recorded by applying an alternating voltage (peak amplitude = 5mV, frequency range = 10^{-2} to 10^5 Hz).
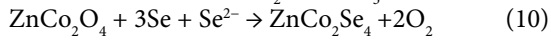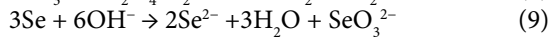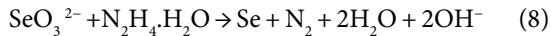
2.3. Synthesis of ZnCoO and ZnCoSe*

In this section, the synthesis procedure for the ZnCoO and ZnCoSe is disclosed in details. First, 5cc Zn(NO$_3$)$_2$·6H$_2$O (0.2 mol.) and 10cc CoCl$_2$·6H$_2$O (0.2 mol.) were added in 1:2 molar ratio to 55cc deionized water. Next, in order to produce ZnCoO, 15cc CO(NH$_2$)$_2$ (0.6 mol.) + 15cc NH$_4$F (0.2 mol.) and in order to produce ZnCoSe, 2cc N$_2$H$_4$.H$_2$O +15

cc Na$_2$SeO$_3$ (0.2 M) were mixed with the previous solution. Meanwhile, nickel foam was cut into small 1 cm^2 pieces then left in a 3 M hydrochloric acid solution, acetone and deionized water each for 30 minutes to become clean and ready. After that, an autoclave was filled by the admixture of the substrates and the solution so that the products precipitate over the foam pieces (180 °C, 5 h). Afterward, the system was allowed to cool down then opened and the electrodes were removed while the chemicals were deposited on the Ni foam pieces surface. Then, they were put in 60 °C oven for a while to dry. Active chemicals weight were calculated using a microbalance (Accuracy = 10 μg, model: ABT-100-5M KERN $ Sohn GmbH, Germany, in this stage because it was required to find C$_{sp.}$

In order to produce ZnCoSe*, another stage followed the first stage in above in which ZnCoO was produced. In this second stage, A nickel foam, coated with ZnCoO, was chosen and put in another solution containing 2cc N$_2$H$_4$.H$_2$O, + 15 cc Na$_2$SeO$_3$ (0.2 M) then similarly to the previous stage transferred into an autoclave at constant 180 °C temperature for 5h. After that, the same procedure was carried out for washing and weighing the precipitate composite. Adding hydrazine and sodium selenite and maintaining the electrodes in this temperature for 5 h gave the chance for substitution of oxygen with selenium in the solution. The production mechanisms for ZnCoO could be as follows:

$$Zn^{2+} + 4OH \rightarrow Zn(OH)_4^{2-} \tag{1}$$
$$Zn(OH)_4^{2-} \rightarrow ZnO + H_2O + 2OH^- \tag{2}$$
$$CO(NH_2)_2 + 2H_2O \rightarrow 2NH_3 + CO_2 \tag{3}$$
$$NH_4F + H_2O \rightarrow OH^- + NH_3 . H_2O + HF \tag{4}$$
$$NH_3 + H_2O \rightarrow NH_4^+ + OH^- \tag{5}$$
$$2Co^{+2} + Zn^{+2} + 6OH^- \rightarrow ZnCo_2(OH)_6 \tag{6}$$
$$ZnCo_2(OH)_6 + 0.5O_2 \rightarrow ZnCo_2O_4 + 3H_2O \tag{7}$$

Moreover, the following chemical reactions could be the mechanism for ZnCoSe formation:

$$SeO_3{}^{2-} + N_2H_4.H_2O \rightarrow Se + N_2 + 2H_2O + 2OH^- \qquad (8)$$

$$3Se + 6OH^- \rightarrow 2Se^{2-} + 3H_2O + SeO_3{}^{2-} \qquad (9)$$

$$ZnCo_2O_4 + 3Se + Se^{2-} \rightarrow ZnCo_2Se_4 + 2O_2 \qquad (10)$$

3. Results and discussion

FE-SEM images of the produced composites in high and low magnifications, are provided in Fig. 1. Fig. 1 a, c, and e show low magnification images of ZnCoO, ZnCoSe, and ZnCoSe*, respectively, and reveal that they consist of highly congregated fine elements. In the case of ZnCoO, the nano-structures have formed distinctive micro-spheres. Fig. 1b shows a high magnification of this image and a closer look into the micro-spheres verifies the presence of blade-like nanostructures that at least one of their dimensions is sub-micron. Plenty of void spaces could be seen in the images of this material that are a sign of its high porosity. The low magnification image of ZnCoSe shows uniformity of this material in a wide range and in the

corresponding zoomed image (Fig. 1d), the surface seems to be highly rough and consisting of many nanostructures in shape of nano-flake that are densely aggregated. The 2-dimensional geometry of this material promises high electrochemical reactivity due to its high surface area [24-26]. Elemental mapping images of the SEM figures were obtained and indicated the homogeneous distribution of the constituting elements in the composites (Fig. 2). Fig. 2 b and c relate to ZnCoSe and ZnCoSe* electrodes and importantly, have the same amount of Se cations.

In order to examine the atomic structure of the produced electrodes, the XRD and FTIR analysis were applied and the results are plotted in Fig. 3. In this figure, distinctive XRD peaks at 2θ values of 31.2˚, 36.8˚, 44.7˚, 55.6˚, 59.3˚, 65.1˚, and 77.2˚ corresponding to (220), (311), (400), (422), (511), (440), and (533) planes of a cubic structure were recorded , respectively (space group: Fd-3 m,
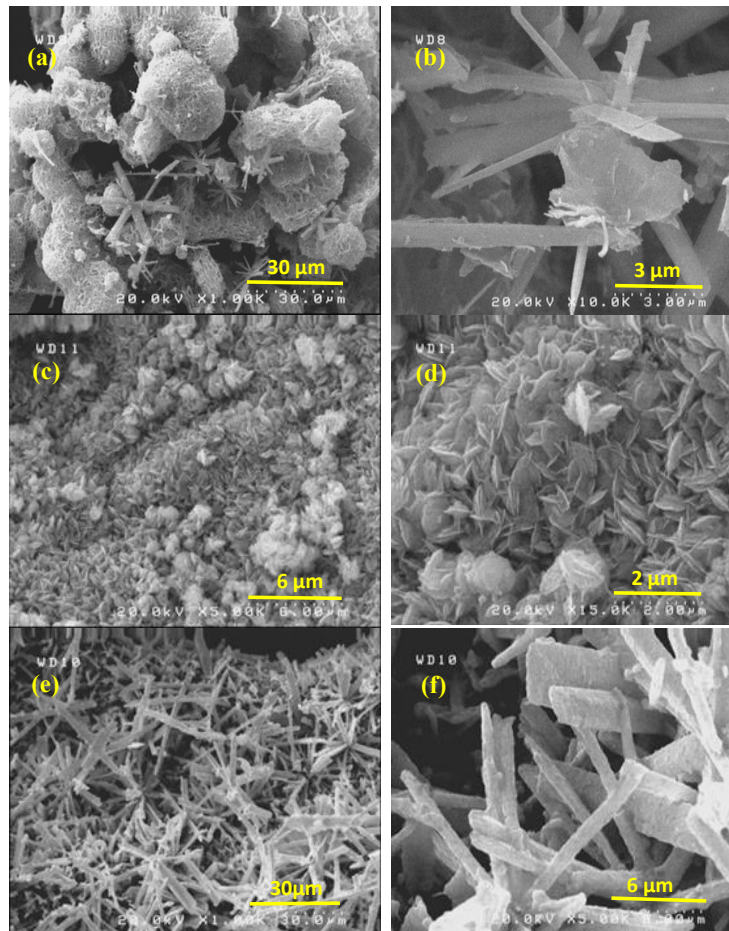

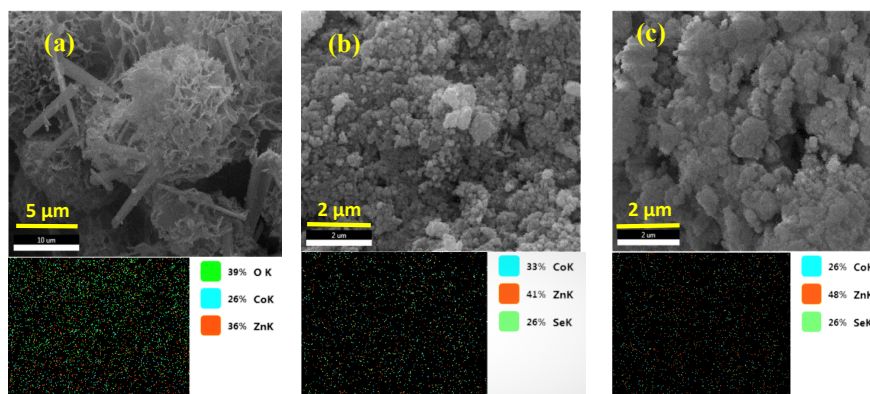Fig. 1- SEM images of the (a, b) ZnCoO, (c, d) ZnCoSe and (e, f) ZnCoSe* electrodes materials.

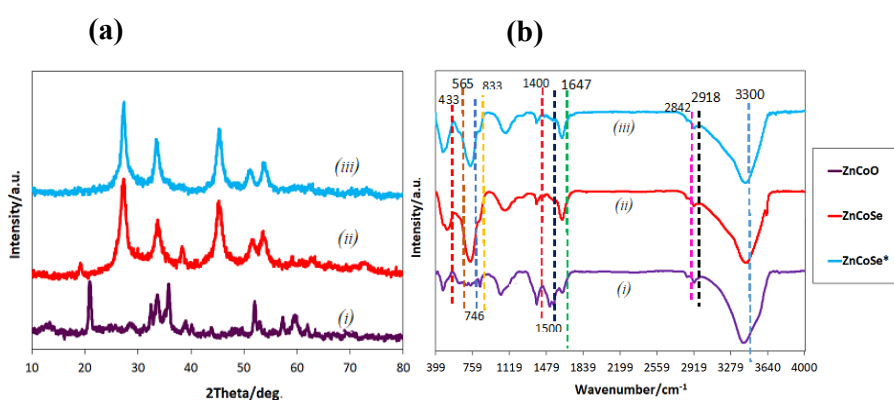Fig. 2- SEM images of the (a, b) ZnCoO, (c, d) ZnCoSe and (e, f) ZnCoSe* electrodes materials.

Fig. 3- (a) XRD and (b) FTIR images of the (i) ZnCoO, (ii) ZnCoSe and (iii) ZnCoSe* electrodes materials.

JCPDS no. 23-1390, a = 8.0946 Å) that are related to crystalline structure of Zn-Co-O bonds [14, 23, 27]. XRD results of ZnCoSe and ZnCoSe* are very similar and confirm their identical chemical combination. Moreover, these figures have peaks at $2\theta = 27.3$ and 45.4 which are related to <111> and <220> planes and were already reported for zinc selenide [28]. In addition to that, they showed peaks at $2\theta = 33.65$, 51.4 and 62.8 corresponding to <210>, <311> and <400> planes which were reported in cobalt selenide before [28-30]. These peaks were confirmed from JCPDS cards no. 88-1718 and 80-0021 and successfully verified that the produced electrodes were a mixture of zinc and cobalt selenides.

Furthermore, the FTIR revealed the chemical bonds and elements in the structure (Fig. 3b). This test affirmed that all the three elements consisted of almost similar bonds with slight alterations which are detectable by comparing the valleys in the plots. The corresponding wave number for each domain is given by a dash line next to it. A tiny FTIR peak

is dominant around 1500 cm^{-1} in the ZnCoO spectrum that is missing in the selenide spectra. This could be a result of the oxygen atoms substitution by the selenium ions. Thereby, this peak could be ascribed to the stretching vibration of the bonds between cobalt/zinc and oxygen atoms. Conversely, a stretching band is only distinguishable at 746 cm^{-1} in the selenides spectra; this could also be a result of addition of the third atom and formation of Zn/Co-Se bonds [31]. The peaks at 3300, 1647, 1500, and 1400 cm^{-1} are signs of the vibrations of C-N, H-N-H, C-H, and H-OH bonds which are formed by the materials used in fabrication procedure. Finally, the peaks apperceived at 2918 and 2840 cm^{1} seem to be possibly related to Zn-Se and Zn-Zn.

The CV test is applied using a three-electrode electrochemical cell in which SCE and platinum sheet were used as the reference and counter electrode respectively. This configuration was used for every CV test in the whole paper. The results of this test for the synthesized electrodes are compared in Fig. 4 in terms of the scan rate,

material and specific capacity. These plots represent the ZnCoO, ZnCoSe and ZnCoSe* CV results at various scan rates between 10 and 100 mV s^{-1}. The pseudocapacitive behavior of the electrodes could be perceived from the presence of the oxidation and reduction peaks in the CV results. Furthermore, some small shifts in these peaks could be identified while it should be noted that they are more easily to be noticed in lower scan rates because the cations and anions would have ample time to penetrate into the deep spaces in low frequencies. Fig. 4d represents comparative charts which show that the ZnCoSe* electrode has the largest area enclosed by the CV curves. This could be observed by calculation of Csp in terms of scan rate too. The C$_{sp}$ calculation results are provided in Fig. 4e and show a descending trend

for all the electrodes as the scan rate rises. However, the ZnCoSe* capacitance is higher than the others irrespective of the scan rate (Fig. 4d). According to this figure, the specific capacitance values for the ZnCoSe*, the most powerful electrode, were 104, 82, 69, 60, 45, 38 F/g in scan rates 20, 30, 40, 50, 70 and 100 mV/s respectively while the highest capacitances of ZnCoSe and ZnCoO electrodes were 62 and 64 F/g at 20 mV/s. Equation 11 was used to calculate the specific capacitance by the CV results (m: active material mass, s: scan rate, ∫I.dV: area enclosed by the diagram):

$$C_{sp} = \frac{\int I.dV}{S.m} \tag{11}$$

To deeply investigate the conduction of synthesized materials, EIS analyses were performed
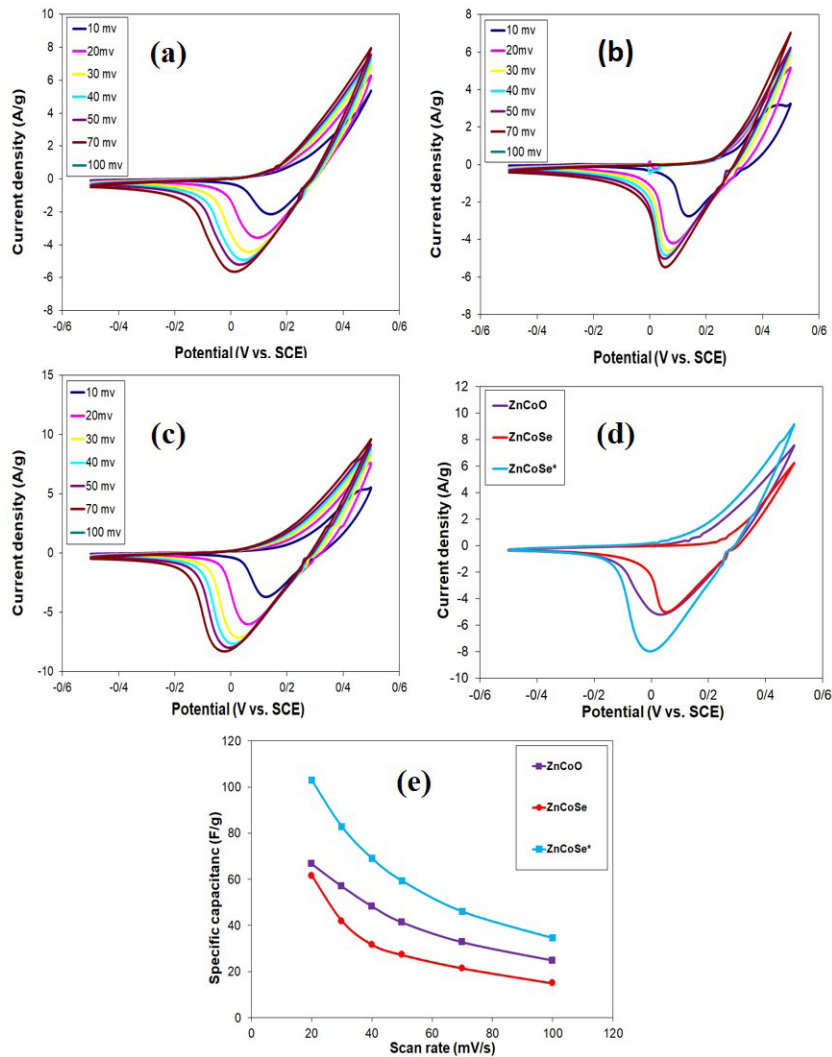

Fig. 4- CVs of (a) ZnCoO, (b) ZnCoSe and (c) ZnCoSe* electrodes materials at different scan rates of 10 up to 200 mV s^{-1}. (d) CVs of all electrode at 50 mV s^{-1} scan rate. (e) Charge storage dependence of composite electrodes as a function of scan rate from 20 to 200 mV s^{-1}.

with an open-circuit potential (f = 10^{-2} to 10^5 Hz) at room temperature and the results are plotted in Fig. 5. Panels a and b in this figure respectively represent the magnitude and phase bode diagrams of the electrodes versus frequency. According to the former, ZnCoSe* has had the lowest impedance magnitude in low frequencies which is a sign of higher conductivity of this electrode. Bearing in mind that phase of an ideal capacitance is -90 degree, it could be understood from Fig. 5(b) that the electrodes had better capacitive properties in low frequencies and the ZnCoSe* electrode was more similar to capacitors than the others in such frequencies.

The Nyquist plots for ZnCoO, ZnCoSe and ZnCoSe* are composed of a semicircle and a tilted straight line, which could be modeled by the equivalent circuit shown in Fig. 5c. The proposed equivalent circuit comprises a series resistance (R_s), a charge-transfer resistance, a Warburg element and a double layer capacitance. R_s models mass transfer in the electrolyte as well as the electrodes intrinsic conductivity and is in series with the whole combination of the rest of elements. R_{ct} is in series with Warburg element and their combination is parallel with the double layer capacitance (C_{dl}).

Based on the inset in the Nyquist panel, the radius of the semi-circle for ZnCoSe and ZnCoSe* are much smaller than ZnCoO that could barely be identified. Moreover, ZnCoSe* intersected the horizontal axis in the smallest value among all the electrodes. The former could be an indication of high charge transfer capability of the ZnCoSe* electrode and the latter could be interpreted as the superiority of it in terms of electrical conductivity. These two pieces of evidence lead us to conclude that the ZnCoSe* electrode had the highest conductivity both in terms of R_s and R_{ct}, which is necessary for high energy density delivery.

The Capacitive nature of the electrodes could be understood from the Nyquist diagram. Faradaic reactions have caused a 45 degree slopped line in the regions far from the origin of the Nyquist diagram. This behaviour stems from the fact that there exists multiple forms of nanoparticles and a high degree of heterogeneity in the electrodes. Therefore, the electrodes are in fact combinations of multiple impaired capacitors that are acting simultaneously and as a result the line in the low frequencies has deviated from an ideal capacitance line: straight and vertical. This line is modeled using a Warburg element which is the dominant
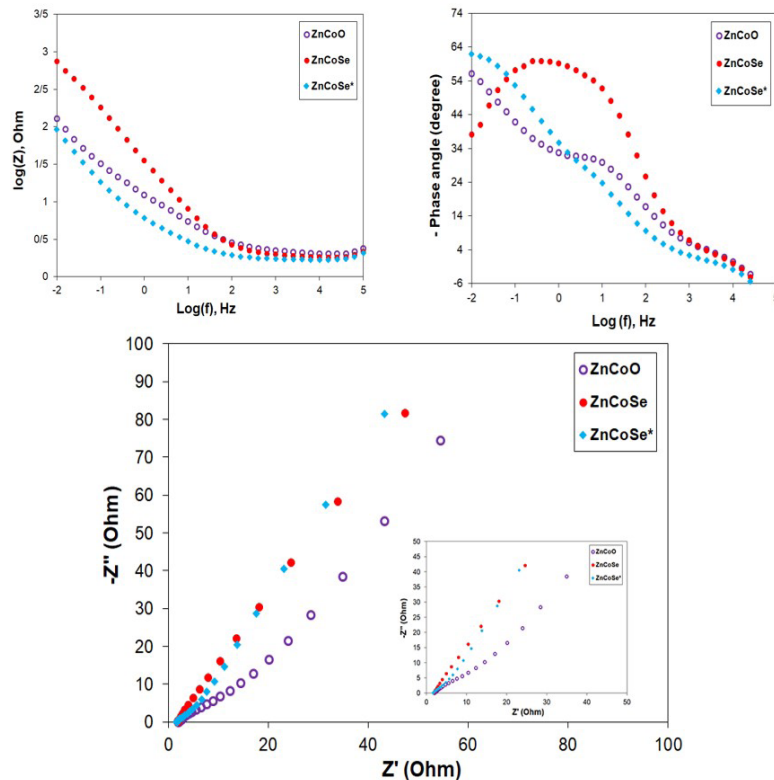
Fig. 5- Impedance spectroscopy plots of electrodes at 100000 to 0.01 Hz sweep. (a) Bode, (b) phase, and (c) Nyquist plots.

Table 2- Equivalent circuit model parameters

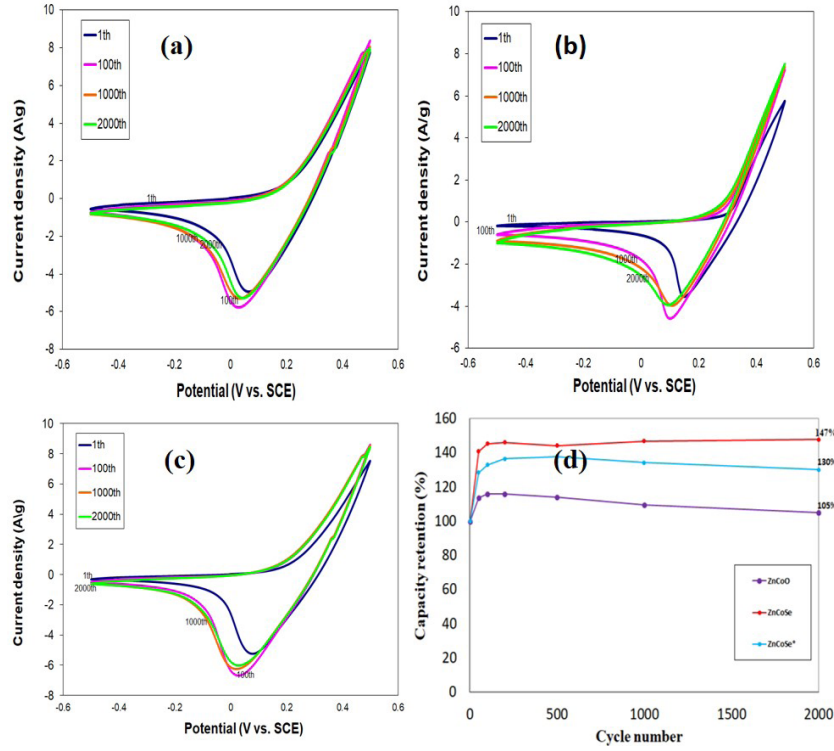| Electrode	R_{ct} (Ω)	Rs (Ω)	CPEt	CPEp	Wr	Wt	Wp
ZnCoSe*	6.5	1.7	0.037	0.65	340	43.3	0.7
ZnCoSe	11	1.847	0.007	0.72	1084	1.43	0.58
ZnCoO	21	2	0.02	0.585	405	47	0.66

Fig. 6- The 1st, 500th, and 1000th cycles for the (a) (a) ZnCoO, (b) ZnCoSe and (c) ZnCoSe* electrodes at scan rates of 100 mV s⁻¹. (e) Variation of the capacity retention of electrodes as a function of cycle number.

element in low frequencies. The Warburg element that is used for this modeling relies on three parameters: W_T, W_P, and W_R and is ruled by this equation:

$$Z = W_R \frac{\tanh((i\omega W_T)^{W_p})}{(i\omega W_T)^{W_p}} \quad (12)$$

On the other hand, the typical EDLC pseudocapacitance characteristics can be seen in the curved lines at the beginning of the Nyquist plot and could be modeled by the double layer capacitance, C_{dl}. This element is better modeled by a constant phase element (CPE) because the curved line in the high frequency is not a perfect semi-circle. This element is determined using two parameters: CPE_T and CPE_P and is governed by a capacitance-like impedance as follows:

$$Z = \frac{1}{CPE_T \times (i\omega)^{CPE_p}} \quad (13)$$

In this equation ω is angular frequency in rad s⁻¹

but CPE_p is a unit less parameter and the unit of CPE_T depends on the CPE_p value.

The obtained values for the different elements discussed above are given in table 2 and were obtained by a fitting procedure under the condition that the consequent error for the elements would be less than 10%. According to this table, ZnCoSe* had the highest conductivity as was inferred directly from the diagrams. Furthermore, this electrode had the highest CPE_T value that has the closest relationship with the electrode capacitance, i.e. the higher capacitance of an electrode, the higher it highest CPE_T. Bearing in mind this point, we can see that the sequence of electrodes in the ascending order of their CPE_T value matches and validates the CV results in Fig. 4(e).

Fig. 6 shows the 1ˢᵗ, 100ᵗʰ, 1000ᵗʰ and 2000ᵗʰ CV cycles for the ZnCoO, ZnCoSe and ZnCoSe* electrodes at 100 mV s⁻¹ scan rate. In all the cases, the area inside the CV curves initially reached a

higher value than the initial cycle however, as a result of overuse, capacity starts to fall from the initial increase gradually which is clear in Fig. 6(d). The reason behind the increase in the first cycles could be ascribed to the increase of active spots on the electrode surface due to infiltration of ions to deep porous areas inside the nanostructures. The highest increase and retention degree belonged to ZnCoSe while ZnCoO was the worst electrode in this experiment. ZnCoSe reaches to 145% initially and maintains its capacity up to the 2000th cycle while the ZnCoSe* and ZnCoO capacitance at the beginning respectively rose to 135% and 117% but then lowered to 130% and 105%. Therefore, it could be concluded that the addition of Se ions ameliorated the challenge of capacity reduction in this type of energy storage however ZnCoSe* seems to be less stable than ZnCoSe. Consequently, this lower degree of cyclability could be considered as the cost of enhanced C$_{sp}$.

The GCD curves of the electrodes are shown in Fig. 7 (0.5 V potential window and 50 mA cm^{-2} charge-discharge current) to compare the electrodes' charge and discharge rate. As can be seen from this figure, ZnCoSe* expectedly had the best charge-discharge performance because it took longer for this electrode to be filled and discharged afterwards. This conclusion corresponds well with our other outcomes in CV and EIS tests where the ZnCoSe* had the highest capacitance.

Fig.8 represents discharge curves of ZnCoSe* at different discharge current densities (10 to 50 mA cm^{-2}). These curves and obtained values are helpful to further investigate the electrochemical storage properties. The specific capacitance value can be

calculated from this figure using this equation:

$$C_s = \frac{I\Delta t}{m\Delta V} \ (F/g) \tag{14}$$

I, m, Δt, ΔV respectively denote discharge current (A), the total mass of electrode materials (g), discharge time (s), voltage window (V). The specific capacitance of ZnCoSe* using this method was calculated to be 150, 206.7, 178.1, 160 and 147.6 F.g^{-1} at 10, 20, 30, 40 and 50 mA cm^2, respectively. This is almost in agreement with our expectation that in higher current densities, the specific capacitance should decrease because of the sluggish movement of ions into the deep areas inside the pores of the nanostructures that is even more critical in higher current densities. This trend was not consistent in the case of increase of current density from 10 to 20 mA cm^{-2} that could be attributed to the fact that after the experiment with 10 mA cm^{-2} current density, electrolyte and ions have found time to infiltrate into the pores and the active area has such increased that has compensated the effect of higher current density and the capacitance has increased as a result. It could be seen that the specific capacitance has decreased as the current density has increased. This The values of specific energy and power are calculated using this figure and are presented in Table 3. The following equations are applied in this regard:

$$E_{sp} = \frac{0.5 \, C_{sp} \, \Delta V^2}{3.6} \ (W.h/kg) \tag{15}$$

$$P_{sp} = \frac{E_{sp}}{\Delta t} \ (W/kg) \tag{16}$$

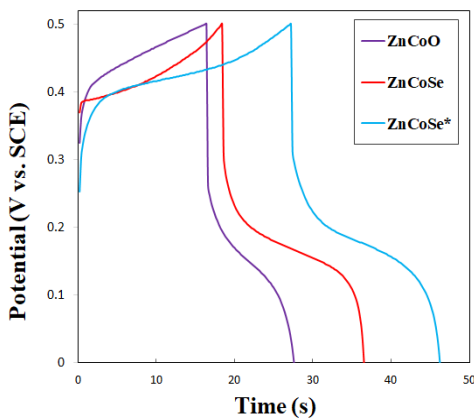In the above equations, ΔV and Δt are the applied

Fig. 7- Galvanostatic charge-discharge curves of electrodes over a potential window between 0 and 0.5 V at 50 mA cm^{-2} charge-discharge current.
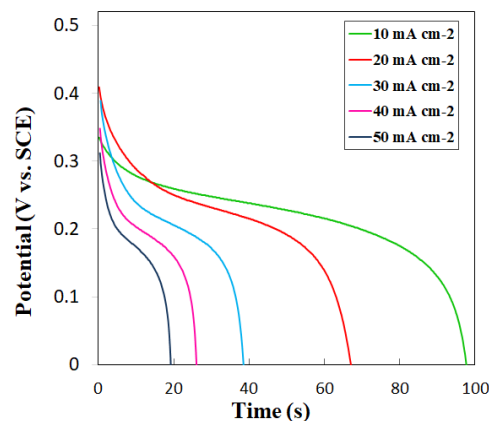

Fig. 8- Discharge curves of ZnCoSe* over a potential window between 0 and 0.5 V at 10, 20, 30, 40 & 50 mA cm^{-2} discharge current.

Table 3- Electrical results for the ZnCoSe* electrode prepared at 180 °C 5h calculated at different charge-discharge current densities

Current density (Acm^{-2})	Discharge time (s)	Specific capacitance (Fg^{-1})	Specific energy ($Whkg^{-1}$)	Specific power (Wkg^{-1})
10	98	150	5.22	191
20	67	207	7.17	385
30	39	178	6.18	570
40	26	160	5.55	768
50	19	148	5.12	970

voltage frame and the discharge time. It should be noted that the batteries are strong devices in storing energy but weak in the power contrary to capacitors which can quickly discharge and transfer their energy to the connected circuit. A similar trend could be also observed in Table III where in the higher discharge currents that the discharge time was lower, the specific energy has decreased while the specific power has increased. Nevertheless, the high specific energy and power that ZnCoSe* provides make it a promising material in applications that require high capacity as well as great energy delivery.

4. Conclusion

In this paper, hydrothermal process was successfully utilized to synthesize mixed zinc cobolt selenide as well as zinc cobolt oxide. An improved method was also introduced for synthesis of zinc cobolt selenide which was comprised of two stages and we called it two-stage synthesis method. Altogether, three electrodes were built, thoroughly examined and compared. Successful coverage of the electrode substrate according to the target chemical combination was confirmed using the elemental map distribution, XRD and FTIR tests. Moreover, their morphology were found to be a mixture of various nanostructures such as nano flakes and microsphere making them highly porous and suitable for storing electric charges. It was discovered that the mixed transition selenide produced through the modified procedure offered better electrochemical performance than the other electrodes. The highest attained specific capacity was 104 F g^{-1} at 20 mV/s and this electrode was capable of preserving its capacity up to 145% after 2000 charge and discharge cycles. Having known promising electrochemical properties of selenides, it could be concluded that this synthesis procedure could be adopted to increase capacity of the formerly built electrodes based on the same material.

References

1. Zardkhoshoui AM, Davarani SSH. Construction of complex copper-cobalt selenide hollow structures as an attractive battery-type electrode material for hybrid supercapacitors. Chemical Engineering Journal. 2020;402:126241.

2. Mohammadi Zardkhoshoui A, Hosseiny Davarani SS. Formation of graphene-wrapped multi-shelled NiGa2O4 hollow spheres and graphene-wrapped yolk–shell NiFe2O4 hollow spheres derived from metal–organic frameworks for high-performance hybrid supercapacitors. Nanoscale. 2020;12(3):1643-56.

3. Li B, Gu P, Feng Y, Zhang G, Huang K, Xue H, et al. Ultrathin Nickel-Cobalt Phosphate 2D Nanosheets for Electrochemical Energy Storage under Aqueous/Solid-State Electrolyte. Advanced Functional Materials. 2017;27(12):1605784.

4. Cheng Y, Zhang Y, Jiang H, Dong X, Meng C, Kou Z. Coupled cobalt silicate nanobelt-on-nanobelt hierarchy structure with reduced graphene oxide for enhanced supercapacitive performance. Journal of Power Sources. 2020;448:227407.

5. Monjoghtapeh RH, Zardkhoshoui AM, Hosseiny Davarani SS. Hierarchical MnCo2S4 nanowires/NiFeLDH nanosheets/graphene: A promising binder-free positive electrode for high-performance supercapacitors. Electrochimica Acta. 2020;338:135891.

6. Mohammadi Zardkhoshoui A, Hosseiny Davarani SS, Maleka Ashtiani M, Sarparast M. Designing an asymmetric device based on graphene wrapped yolk–double shell NiGa2S4 hollow microspheres and graphene wrapped FeS2FeSe2 core–shell cratered spheres with outstanding energy density. Journal of Materials Chemistry A. 2019;7(17):10282-92.

7. Chen T-Y, Lin L-Y. Morphology variation for the nickel cobalt molybdenum copper oxide with different metal ratios and their application on energy storage. Electrochimica Acta. 2019;298:745-55.

8. Mohammadi Zardkhoshoui A, Hosseiny Davarani SS. Ultra-high energy density supercapacitors based on metal–organic framework derived yolk–shell Cu–Co–P hollow nanospheres and CuFeS2 nanosheet arrays. Dalton Transactions. 2020;49(10):3353-64.

9. Jiang Y, Ma X, Feng J, Xiong S. Selenium in nitrogen-doped microporous carbon spheres for high-performance lithium–selenium batteries. Journal of Materials Chemistry A. 2015;3(8):4539-46.

10. Ma F, Lu J, Pu L, Wang W, Dai Y. Construction of hierarchical cobalt-molybdenum selenide hollow nanospheres architectures for high performance battery-supercapacitor hybrid devices. Journal of Colloid and Interface Science. 2020;563:435-46.

11. Mohammadi Zardkhoshoui A, Hosseiny Davarani SS. Boosting the energy density of supercapacitors by encapsulating a multi-shelled zinc–cobalt-selenide hollow nanosphere cathode and a yolk–double shell cobalt–iron-selenide hollow nanosphere anode in a graphene network. Nanoscale.

2020;12(23):12476-89.

12. Luo M, Yu H, Hu F, Liu T, Cheng X, Zheng R, et al. Metal selenides for high performance sodium ion batteries. Chemical Engineering Journal. 2020;380:122557.

13. Xu L, Zhao Y, Lian J, Xu Y, Bao J, Qiu J, et al. Morphology controlled preparation of ZnCo 2 O 4 nanostructures for asymmetric supercapacitor with ultrahigh energy density. Energy. 2017;123:296-304.

14. Wang Y, Zhao C, Fu W, Zhang Z, Zhang M, Zhou J, et al. Growth of zinc cobaltate nanoparticles and nanorods on reduced graphene oxide porous networks toward high-performance supercapacitor electrodes. Journal of Alloys and Compounds. 2016;668:1-7.

15. Kathalingam A, Ramesh S, Yadav HM, Choi J-H, Kim HS, Kim H-S. Nanosheet-like ZnCo2O4@nitrogen doped graphene oxide/polyaniline composite for supercapacitor application: Effect of polyaniline incorporation. Journal of Alloys and Compounds. 2020;830:154734.

16. Jadhav HS, Roy A, Chung W-J, Seo JG. Growth of urchin-like ZnCo2O4 microspheres on nickel foam as a binder-free electrode for high-performance supercapacitor and methanol electro-oxidation. Electrochimica Acta. 2017;246:941-50.

17. Nguyen TT, Balamurugan J, Aravindan V, Kim NH, Lee JH. Boosting the energy density of flexible solid-state supercapacitors via both ternary NiV2Se4 and NiFe2Se4 nanosheet arrays. Chemistry of Materials. 2019 May 23;31(12):4490-504.

18. Li L, Zhao J, Zhu Y, Pan X, Wang H, Xu J. Bimetallic Ni/Co-ZIF-67 derived NiCo2Se4/N-doped porous carbon nanocubes with excellent sodium storage performance. Electrochimica Acta. 2020;353:136532.

19. Cheng L, Chen S, Zhang Q, Li Y, Chen J, Lou Y. Hierarchical sea-urchin-like bimetallic zinc–cobalt selenide for enhanced battery-supercapacitor hybrid device. Journal of Energy Storage. 2020;31:101663.

20. Chebrolu VT, Balakrishnan B, Chinnadurai D, Kim HJ. Selective Growth of Zn–Co–Se Nanostructures on Various Conductive Substrates for Asymmetric Flexible Hybrid Supercapacitor with Enhanced Performance. Advanced Materials Technologies. 2020;5(2):1900873.

21. Xu G, Zhang Z, Qi X, Ren X, Liu S, Chen Q, et al. Hydrothermally synthesized FeCo2O4 nanostructures: Structural manipulation for high-performance all solid-state supercapacitors. Ceramics International. 2018;44(1):120-7.

22. Pawar ST, Chavan GT, Prakshale VM, Sikora A, Pawar SM, Kamble SS, et al. Physical, structural and topographical aspects of Zn1−xCoxSe thin films. Materials Science in Semiconductor Processing. 2017;61:71-8.

23. Sharma Y, Sharma N, Subba Rao GV, Chowdari BVR. Nanophase ZnCo2O4 as a High Performance Anode Material for Li-Ion Batteries. Advanced Functional Materials. 2007;17(15):2855-61.

24. Meng Z, Xu J, Yu P, Hu X, Wu Y, Zhang Q, et al. Double perovskite La2CoMnO6 hollow spheres prepared by template impregnation for high-performance supercapacitors. Chemical Engineering Journal. 2020;400:125966.

25. Jia H, Wang J, Fu W, Hu J, Liu Y. In-situ MOFs-derived hollow Co9S8 polyhedron welding on the top of MnCo2S4 nanoneedles for high performance hybrid supercapacitors. Chemical Engineering Journal. 2020;391:123541.

26. Han X, Chen Q, Zhang H, Ni Y, Zhang L. Template synthesis of NiCo2S4/Co9S8 hollow spheres for high-performance asymmetric supercapacitors. Chemical Engineering Journal. 2019;368:513-24.

27. Jin J, Zheng Y, Kong LB, Srikanth N, Yan Q, Zhou K. Tuning ZnSe/CoSe in MOF-derived N-doped porous carbon/CNTs for high-performance lithium storage. Journal of Materials Chemistry A. 2018;6(32):15710-7.

28. Majhi KC, Karfa P, De S, Madhuri R. Hydrothermal Synthesis of Zinc Cobalt Telluride Nanorod towards Oxygen Evolution Reaction (OER). IOP Conference Series: Materials Science and Engineering. 2019;577(1):012076.

29. Pawar ST, Chavan GT, Prakshale VM, Sikora A, Pawar SM, Kamble SS, et al. Solution grown ZnSe:Co nanocrystalline thin films: The characteristic properties. AIP Conference Proceedings: Author(s); 2018.

30. Zhang Z, Huang Y, Liu X, Wang X, Liu P. Core–Shell Co, Zn Bimetallic Selenide Embedded Nitrogen-Doped Carbon Polyhedral Frameworks Assist in Sodium-Ion Battery Ultralong Cycle. ACS Sustainable Chemistry & Engineering. 2020;8(22):8381-90.

31. Raut SS, Sankapal BR. First report on synthesis of ZnFe2O4 thin film using successive ionic layer adsorption and reaction: Approach towards solid-state symmetric supercapacitor device. Electrochimica Acta. 2016;198:203-11.